Spin−Orbit Torque in Bilayers of Kagome Ferromagnet Fe$_3$Sn$_2$ and Pt

Igor Lyalin,[‡] Shuyu Cheng,[‡] and Roland K. Kawakami*

Read Online

ACCESS | Metrics & More | Article Recommendations | SI Supporting Information

ABSTRACT: Spin−orbit torque phenomena enable efficient manipulation of the magnetization in ferromagnet/heavy metal bilayer systems for prospective magnetic memory and logic applications. Kagome magnets are of particular interest for spin−orbit torque due to the interplay of magnetic order and the nontrivial band topology (e.g., flat bands and Dirac and Weyl points). Here we demonstrate spin−orbit torque and quantify its efficiency in a bilayer system of topological kagome ferromagnet Fe$_3$Sn$_2$ and platinum. We use two different techniques, one based on the quasistatic magneto-optic Kerr effect (MOKE) and another based on time-resolved MOKE, to quantify spin−orbit torque. Both techniques give a consistent value of the effective spin Hall angle of the Fe$_3$Sn$_2$/Pt system. Our work may lead to further advances in spintronics based on topological kagome magnets.

KEYWORDS: spin−orbit torque, magneto-optic Kerr effect, kagome ferromagnet, magnetization dynamics
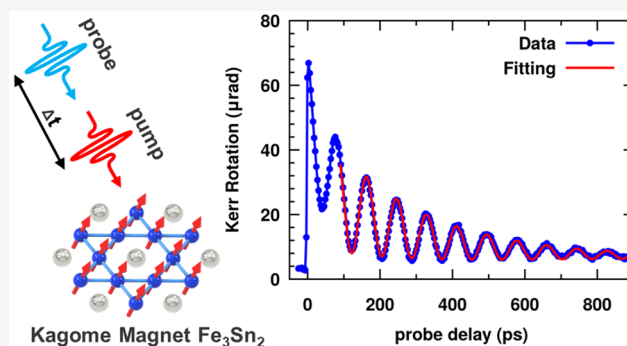
INTRODUCTION

Magnetic materials with kagome crystal structure have attracted great attention as they have been shown to host many exotic phenomena. On one hand, these materials are of interest as they exhibit frustrated ferromagnetic or antiferromagnetic order,[1−3] spin liquid phases,[4,5] and skyrmion formation.[6−10] On the other hand, they are interesting due to a topologically nontrivial electronic band structure with Weyl nodes, Dirac cones, and flat bands.[11−14] The underlying Berry curvature of these topological features gives rise to various emergent phenomena, such as large anomalous Hall effect (AHE),[3,15−17] anomalous Nernst effect (ANE),[18−20] and chiral anomaly.[11,21] Unlike the case of ordinary nonmagnetic materials, the band structures of kagome magnets are not only determined by the crystal structure but also strongly dependent on the magnetic state.[11,22,23] Therefore, the manipulation of a magnetic state would lead to control over the band topology and allow for the development of technology and fundamental science based on topological states. An important next step is to show that magnetic moments in topological kagome materials can be efficiently manipulated electrically.

Spin−orbit interaction allows conversion between charge current and spin current. It gives rise to the spin−orbit torque (SOT) phenomena that have been extensively studied and shown to be an efficient way to manipulate magnetization of ferromagnets.[24] When a ferromagnet (FM) is interfaced with a heavy metal (HM), spin current generated by the spin Hall effect in the bulk of the HM or by the Rashba−Edelstein effect at the interface can exert torques on magnetic moments, which manipulate the magnetization dynamics,[25] drive domain walls and skyrmions[26,27] and even switch the magnetization.[28−30] The SOT is expected to lead to logic and memory device applications with high energy efficiency.[24,31,32] However, until now, due to difficulties in the synthesis of thin films, there are only two reports to our knowledge on SOT phenomena in topological kagome materials (both Mn$_3$Sn).[33,34]

In this letter, we report the observation of spin−orbit torque in a bilayer system of one of the most interesting kagome ferromagnets Fe$_3$Sn$_2$[8,12,15,20] and an archetypical heavy metal Pt. This is enabled by the recent advance in the synthesis of epitaxial Fe$_3$Sn$_2$ (0001)/Pt (111) bilayers on Al$_2$O$_3$ (0001) substrates by molecular beam epitaxy.[35] The SOT efficiency is quantified using two different techniques based on the magneto-optic Kerr effect (MOKE) to measure the effective spin Hall angle in Fe$_3$Sn$_2$/Pt bilayers. The values of the effective spin Hall angle obtained from a quasistatic MOKE experiment with a slow ac modulation agree with a time-resolved MOKE experiment that monitors magnetization
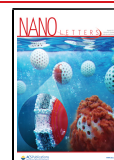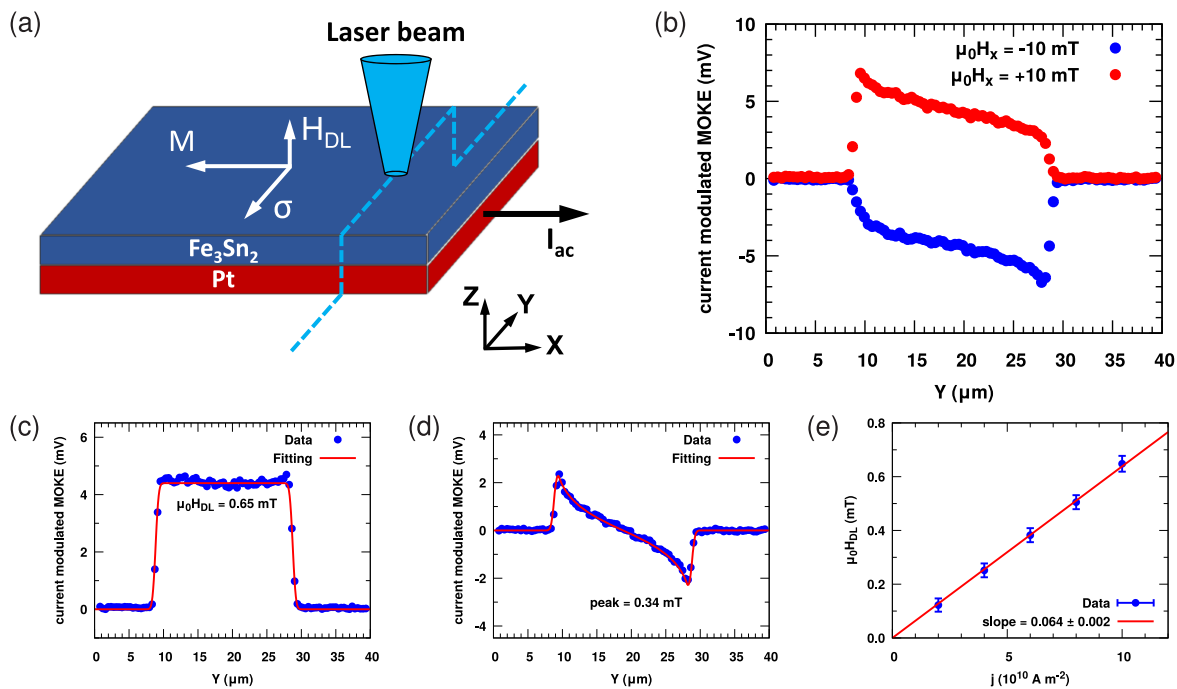
Figure 1. DL-SOT detected by current-modulated polar MOKE. (a) Schematic of experimental setup for using polar MOKE to detect the DL-SOT. An ac current through the sample along the X direction generates DL-SOT, which rotates the magnetization by a small angle out-of-plane, which is detected by MOKE using a lock-in amplifier. (b) Example of a line scan across the channel of the Fe_3Sn_2/Pt (5/5 nm) device, with the ac current density $j = 10^{11}$ A/m^2 applied to the channel. (c) Half difference of the current modulated MOKE voltages shown in (b) $[V(+10 \text{ mT}) - V(-10 \text{ mT})]/2$ measures the effective DL-SOT field, H_{DL}. (d) Half sum $[V(+10 \text{ mT}) + V(-10 \text{ mT})]/2$ of the current modulated MOKE voltages shown in (b) that corresponds to the out-of-plane Oersted field. (e) Linear dependence of effective DL-SOT field vs ac current density, yielding a slope of $\mu_0 H_{DL}/j = (6.4 \pm 0.2)$ mT per 10^{12} A/m^2.

dynamics on the picosecond time scale. We also find that the damping-like (DL) SOT is considerably stronger (∼20 times) than the field-like (FL) SOT. These results promote the development of spintronic devices based on topological kagome magnets.

■ RESULTS AND DISCUSSION

Quasistatic MOKE. Polar MOKE is sensitive to the perpendicular component of magnetization, making it an ideal technique to detect the out-of-plane magnetization induced by the DL-SOT in samples with in-plane magnetic easy axes. Following Fan et al.,[36] we quantify the DL-SOT efficiency using the experimental setup shown in Figure 1a. A Fe_3Sn_2/Pt (5/5 nm) bilayer grown by molecular beam epitaxy (Supporting Information, SI Section 1) is patterned into a 20 μm wide channel (SI Section 2). An alternating current I_{ac} is applied to the channel. When Fe_3Sn_2 is magnetized along the channel, the spin current generated in Pt induces DL-SOT on the Fe_3Sn_2 magnetization, making it rotate a small angle out-of-plane. This can be viewed as an effective magnetic field $\mathbf{H_{DL}} \sim (\mathbf{m} \times \boldsymbol{\sigma})$ oriented out-of-plane, where $\mathbf{m}$ is the normalized magnetization vector and $\boldsymbol{\sigma}$ is the normalized spin polarization vector. The out-of-plane component m_z induced by DL-SOT is detected by polar MOKE using a linearly polarized laser beam at normal incidence. The laser light reflected from the sample is passed through polarization optics to a balanced photo-detector, which outputs a voltage proportional to the Kerr rotation angle. Since the DL-SOT is proportional to the current, the MOKE voltage is proportional to the applied current I_{ac} and can be measured with a lock-in amplifier. Further details of the measurement are in SI Section 3. In

addition, in SI Section 4, we show that the possible contribution from quadratic MOKE,[37] which is sensitive to $m_x m_y$, is negligible for Fe_3Sn_2/Pt.

Figure 1b shows an example of the signal for a Fe_3Sn_2/Pt (5/5 nm) bilayer with ac current density of $j = 10^{11}$ A/m^2 (rms) applied to the channel. The laser beam is scanned across the channel and current-modulated MOKE voltages are recorded at the positive saturation field $V(+H_x)$ and negative saturation field $V(-H_x)$. From these line scans, the signals that originate from the DL-SOT and the out-of-plane Oersted field can be separated, as they have different symmetries. The H_{DL} switches sign as the magnetization switches at the positive and negative saturation fields, while the out-of-plane Oersted field $H_{OOP}^{Oersted}$ is independent of the magnetization. Therefore, the half difference of the MOKE voltages $[V(+H_x) - V(-H_x)]/2$ corresponds to H_{DL} (Figure 1c), while the half sum $[V(+H_x) + V(-H_x)]/2$ corresponds to $H_{OOP}^{Oersted}$ (Figure 1d). As expected, the DL-SOT contribution to the signal is uniform along the line scan, while the out-of-plane Oersted component has different polarities on the opposite edges of the channel. We determine the magnitude of H_{DL} through a calibration against $H_{OOP}^{Oersted}$ calculated from Ampere's law.[36] To account for the finite size of the laser beam, the fitting of the DL-SOT line scan (red curve, Figure 1c) includes a convolution with the laser intensity profile that is modeled as a Gaussian with a radius of 0.5 μm. Fitting the out-of-plane Oersted field line scan (red curve, Figure 1d) is done using a convolution of the Oersted field calculated from Ampere's law, $H_{OOP}^{Oersted}(y) = \frac{I_{ac}}{2\pi w} \ln \frac{w-y}{y}$ with the same Gaussian laser beam, where w is the channel width, y is the laser spot position, $y \in [0, w]$, and I_{ac} is the rms
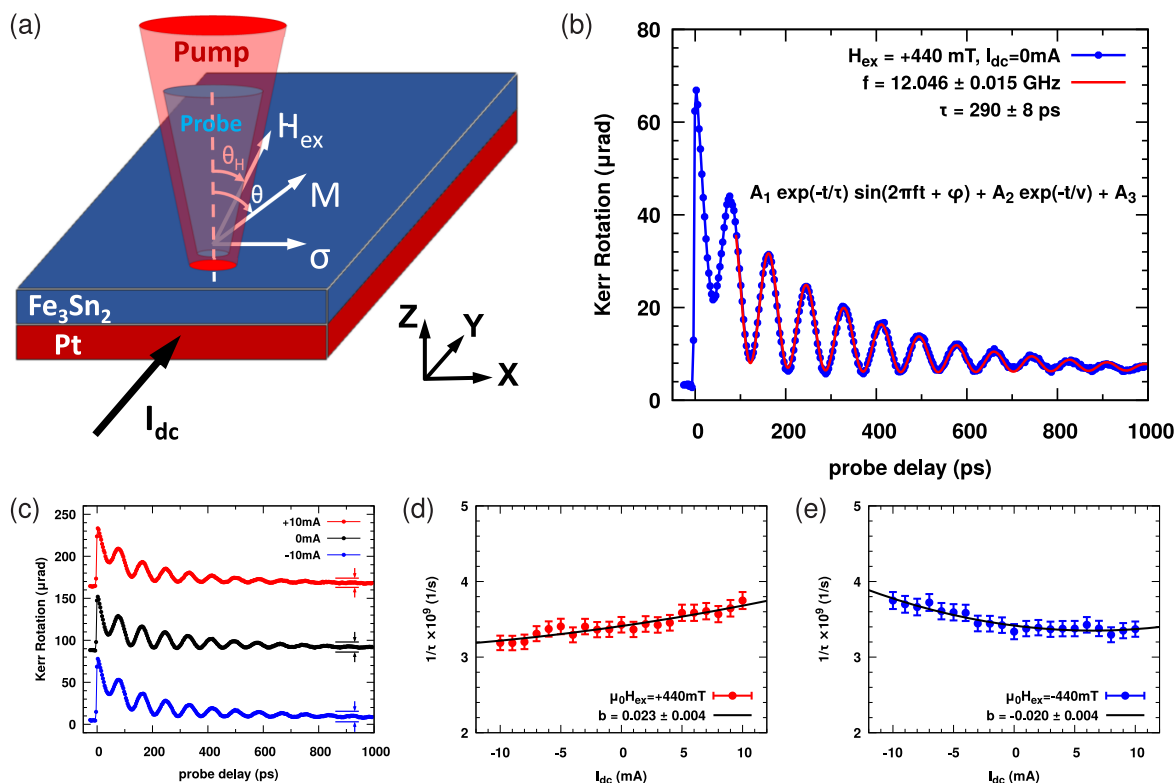
Figure 2. DL-SOT detected by time-resolved MOKE in the "standard geometry." (a) Schematic of the experimental setup for using a change in the relaxation rate of TR-MOKE oscillations to quantify DL-SOT. An external field H_{ex} is applied at $\theta_H = 35°$ from the normal in the XZ plane, a dc current I_{dc} through the sample is applied along Y. (b) Example of the TR-MOKE signal for $\mu_0 H_{ex} = +440$ mT, $I_{dc} = 0$ mA, and its fitting with eq 2. (c) TR-MOKE signal for $I_{dc} = -10$ mA, 0 mA, +10 mA. A slight change in the relaxation rate τ^{-1} (the magnetization oscillations are damped faster for +10 mA current than for −10 mA current) can be barely noticed by the eye without the fitting procedure shown in (b). (d) Dependence of the TR-MOKE relaxation rate τ^{-1} vs dc current I_{dc} applied through the channel, for $\mu_0 H_{ex} = +440$ mT (e) for $\mu_0 H_{ex} = -440$ mT. The fitting functions are quadratic polynomials $aI_{dc}^2 + bI_{dc} + c$.

ac current through the channel. This yields a calibration of 0.148 mT per mV and a value of $\mu_0 H_{DL} = 0.65 \pm 0.03$ mT for $j = 10^{11}$ A/m^2 in Figure 1c. We assume that all of the current flows through the Pt layer, as the resistivity of Fe$_3$Sn$_2$ is much greater than that of Pt, which produces a slight underestimation of the effective spin Hall angle (SI Section 2). Next, we repeat the measurement of H_{DL} for different ac currents. Figure 1e shows that the response is linear and allows us to extract the value of $\mu_0 H_{DL}/j = 6.4 \pm 0.2$ mT per 10^{12} A/m^2.

Assuming that the SOT is generated by the spin Hall effect, we determine the effective spin Hall angle θ_{SH} using the equation[38,39]

$$\frac{\mu_0 H_{DL}}{j} = \frac{\hbar}{2e}\frac{\theta_{SH}}{M_s t_{FM}} \qquad (1)$$

where M_s is the saturation magnetization ($M_s = 610 \pm 20$ kA/m[7,12,20]) and t_{FM} is the thickness of the ferromagnet Fe$_3$Sn$_2$ (5 nm). The effective spin Hall angle in the Fe$_3$Sn$_2$/Pt bilayer is found to be $\theta_{SH} = 0.059 \pm 0.010$. We call θ_{SH} the effective spin Hall angle because θ_{SH} is determined not only by the spin Hall angle but also by the spin transparency of the Fe$_3$Sn$_2$/Pt interface and a damping-like SOT generated at the interface (e.g., a possible damping-like contribution from the Rashba–Edelstein effect).

Time-Resolved MOKE. *Damping Modulation due to DL-SOT.* We next investigate the effect of SOT on magnetization dynamics using the time-resolved magneto-optical Kerr effect (TR-MOKE). Excitation by a linearly polarized pump pulse

(800 nm, 150 fs, 20 mW, ∼4 μm spot size) triggers precessional dynamics of the magnetization, which is detected using the Kerr rotation of a linearly polarized probe pulse (400 nm, 150 fs, 0.5 mW, ∼2 μm spot size) as a function of the pump−probe time delay. A dc current I_{dc} is applied to generate SOT which modifies the magnetization dynamics. Details of the experimental setup are in SI Section 5.

Figure 2b shows a typical TR-MOKE time delay scan measured on the Fe$_3$Sn$_2$/Pt (5/5 nm) bilayer device. In the first few hundred femtoseconds, heating by the pump pulse decreases the magnitude of the magnetization **M** via ultrafast demagnetization[40] and changes the magnetic anisotropy, causing **M** to tilt away from the equilibrium direction. This is followed by a recovery of the magnitude of **M** as the heat is diffused,[41] and the direction of **M** spirals back to the initial equilibrium direction via damped precession governed by the Landau−Lifshitz−Gilbert equation. The magnetization dynamics are evaluated by fitting the TR-MOKE data using

$$\theta_K(t) = A_1 \exp(-t/\tau) \sin(2\pi f t + \varphi)$$
$$+ A_2 \exp(-t/\nu) + A_3 \qquad (2)$$

where τ is the relaxation time and f is the precessional frequency. In the presence of an electrical current, the magnetization dynamics can be described using the Landau−Lifshitz−Gilbert−Slonczewski (LLGS) equation, which includes the effect of spin−orbit torques:
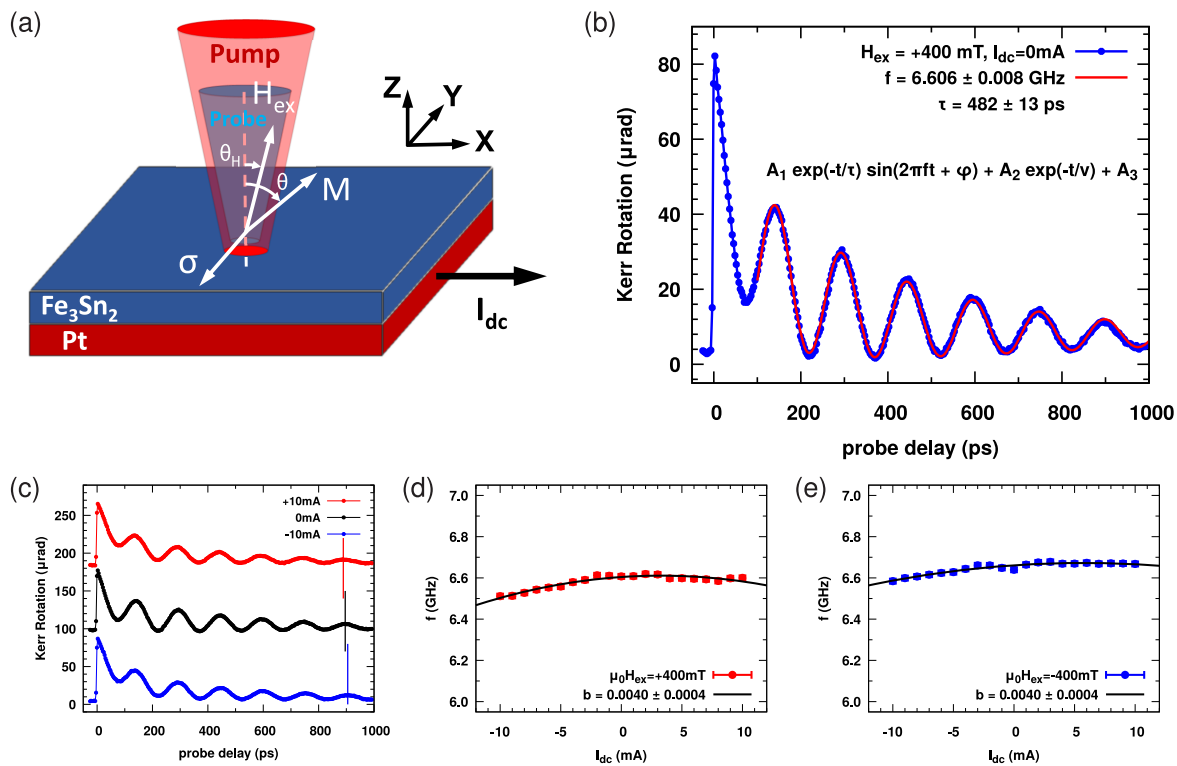
Figure 3. DL-SOT detected by time-resolved Kerr rotation in the "rotated geometry". (a) Schematic of the experimental setup for using a change in the frequency of TR-MOKE oscillations to quantify the DL-SOT. An external field H_{ex} is applied at $\theta_H = 15°$ from the normal in the XZ plane, a dc current I_{dc} through the sample is applied along X. (b) Example of TR-MOKE signal for $\mu_0 H_{ex} = +400$ mT, $I_{dc} = 0$ mA, and its fitting with eq 2. (c) TR-MOKE signal for $I_{dc} = -10$ mA, 0 mA, +10 mA. A slight change in the precessional frequency f (the magnetization precesses faster for +10 mA than for −10 mA dc current) can be barely noticed by the eye without the fitting procedure shown in (b). (d) Dependence of the TR-MOKE frequency f vs dc current I_{dc} applied through the channel, for $\mu_0 H_{ex} = +400$ mT and (e) $\mu_0 H_{ex} = -400$ mT. The fitting functions are quadratic polynomials.

$$\frac{d\mathbf{m}}{dt} = -\gamma\mu_0\mathbf{m} \times \mathbf{H_{eff}} + \alpha\mathbf{m} \times \frac{d\mathbf{m}}{dt} - \gamma\mu_0 H_{FL}\mathbf{m} \times \boldsymbol{\sigma}$$
$$- \gamma\mu_0 H_{DL}\mathbf{m} \times (\mathbf{m} \times \boldsymbol{\sigma}) \tag{3}$$

where $\mathbf{m}$ is the unit vector of magnetization, $\boldsymbol{\sigma}$ is the unit vector of spin polarization, $\mathbf{H_{eff}}$ is the effective magnetic field that includes the external field and effective demagnetizing field (SI Section 2), α is the Gilbert damping constant, and γ is the gyromagnetic ratio. The third term is the field-like spin–orbit torque, which has the same functional form as the precessional term (first term) and is quantified by the effective FL-SOT field H_{FL}. The fourth term is the damping-like spin–orbit torque, which has the same functional form as the damping term (second term, with $d\mathbf{m}/dt \sim \mathbf{m} \times \mathbf{H_{eff}}$) and is quantified by the effective DL-SOT field H_{DL}. The Oersted field generated by the electrical current is treated separately as discussed in SI Sections 7 and 8. The following discussion provides a simplified picture with a minimal set of equations, while the detailed analysis of eq 3 is provided in SI Section 8.

Considering the case without electrical current, the precessional frequency f and the relaxation time τ are given by the following equations for ferromagnetic resonance:[42]

$$\frac{1}{\tau} = \frac{1}{2}\gamma\mu_0\alpha(H_1 + H_2) \tag{4}$$

$$f = \frac{\gamma\mu_0}{2\pi}\sqrt{H_1 H_2} \tag{5}$$

$$H_1 = H_{ex}\cos(\theta - \theta_H) - M_{eff}\cos^2(\theta) \tag{6}$$

$$H_2 = H_{ex}\cos(\theta - \theta_H) - M_{eff}\cos(2\theta) \tag{7}$$

Here, H_{ex} is the applied external magnetic field, M_{eff} is the effective demagnetizing field, θ_H is the angle of the external field, and θ is the angle of the magnetization in the equilibrium state.

Applying an electrical current will generate SOT and produce changes in the magnetization dynamics. In the experimental setup shown in Figure 2a ("standard geometry"), the DL-SOT modulates the relaxation time[43,44] and the FL-SOT modulates the frequency (we discuss DL-SOT here and FL-SOT in SI Sections 7 and 8). For DL-SOT, this geometry maximizes the modulation of the relaxation time. An external magnetic field is applied at an angle $\theta_H = 35° \pm 2°$ from the film normal, with the in-plane component being perpendicular to the device channel and, as a result, to the applied dc current. The angle of the magnetization direction in an equilibrium state θ is determined by the external magnetic field and effective demagnetizing field. θ can be calculated based on the balance between the Zeeman energy and the effective demagnetizing energy:

$$2H_{ex}\sin(\theta - \theta_H) - M_{eff}\sin(2\theta) = 0 \tag{8}$$

The effective demagnetizing field M_{eff} was determined from the anomalous Hall effect measurement (SI Section 2) and found to be 340 ± 10 mT. Figure 2b shows the obtained TR-MOKE data and its fitting by eq 2 for the external field of +440 mT
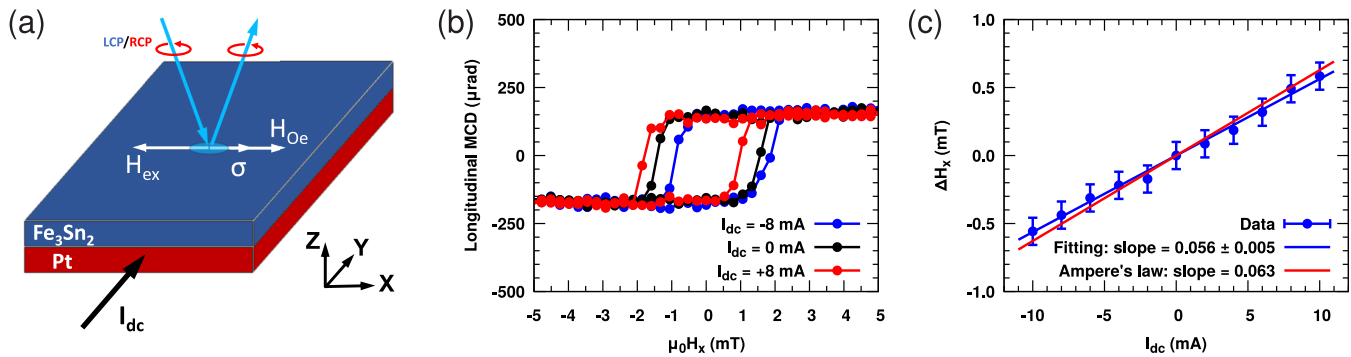
Figure 4. In-plane Oersted field and FL-SOT detected by longitudinal MCD. (a) Schematics of longitudinal MCD. (b) Current-induced shift of the H_x hysteresis loop. (c) Measured current-induced in-plane field extracted from the hysteresis loop shift ΔH_x vs in-plane Oersted field calculated from Ampere's law.

applied at the angle of 35°, in the absence of dc current. The measured frequency of the TR-MOKE oscillations $f \sim 12.0$ GHz agrees with the frequency calculated from eq 5 using the experimental values of M_{eff}, H_{ex}, and θ_H. In the presence of dc current, the damping-like SOT $\sim \mathbf{m} \times (\mathbf{m} \times \boldsymbol{\sigma})$ acts partially collinearly with the damping term in the LLGS equation (eq 3) to increase or decrease the effective damping depending on the polarity of σ. This modulation of the damping or relaxation rate (τ^{-1}) is determined by eqs 1, 3, and 4 and is given by

$$\frac{d\tau^{-1}}{dI_{dc}} = \frac{\gamma\hbar}{2e}\frac{\theta_{SH}}{M_s t_{FM} t_{HM} w}\sin\theta \qquad (9)$$

where t_{HM} is the thickness of the heavy metal Pt film (5 nm) and w is the width of the channel (10 μm). Therefore, the efficiency of DL-SOT can be determined from the modulation of τ^{-1} by the electrical current.

Experimentally, we observe that the magnetization dynamics measured by TR-MOKE exhibits a change in the relaxation rate due to the DL-SOT. Figure 2c shows representative time delay scans measured for dc currents of +10 mA (red curve), 0 mA (black curve), and −10 mA (blue curve) for a positive field $\mu_0 H_{ex} = +440$ mT. The oscillations show a slightly stronger damping for the positive current (red curve) than for the negative current (blue curve) due to the presence of DL-SOT. This trend is consistent with a positive sign of the effective spin Hall angle. Figure 2d shows the dependence of the relaxation rate on the dc current ranging from −10 to +10 mA for the positive field $\mu_0 H_{ex} = +440$ mT. To check that the linear modulation of the relaxation rate is consistent with the DL-SOT, we reverse the external magnetic field. Figure 2e shows the current dependence of the relaxation rate for $\mu_0 H_{ex} = -440$ mT. The reversal of the magnetic field changes the sign of the linear slope $b = d\tau^{-1}/dI_{dc}$ as expected for DL-SOT. This is because under field reversal which also reverses the magnetization, the damping and DL-SOT terms transform with opposite parity: $\mathbf{m} \times (\mathbf{m} \times \mathbf{H}_{eff}) \rightarrow -\mathbf{m} \times (\mathbf{m} \times \mathbf{H}_{eff})$, $\mathbf{m} \times (\mathbf{m} \times \boldsymbol{\sigma}) \rightarrow +\mathbf{m} \times (\mathbf{m} \times \boldsymbol{\sigma})$. The obtained data in Figure 2d,e are fitted using quadratic polynomials $aI_{dc}^2 + bI_{dc} + c$. The parabolic term aI_{dc}^2 accounts for Joule heating which is independent of the current polarity. This term shows increased damping at elevated temperatures, similar to behavior observed in W/CoFeB.[45] Using the obtained experimental value of b, the effective spin Hall angle is calculated to be $\theta_{SH} = 0.065 \pm 0.014$ (SI Section 8). The other values used for the calculation are $\gamma = 185 \pm 18$ GHz/T (we assume a g factor of 2.1,

because for transition metal magnets g lies in the range of 2.0–2.2[42,46,47]), $\mu_0 M_{eff} = 340 \pm 10$ mT, and $M_s = 610 \pm 20$ kA/m.[7,12,20]

Frequency Modulation due to DL-SOT. Next, we discuss the DL-SOT induced change in the frequency of the magnetization precession, that was recently demonstrated by Ishibashi et al.[45] for W/CoFeB bilayers. The experimental setup is shown in Figure 3a ("rotated geometry"), which has a 90° rotation of the device compared to the standard geometry (Figure 2a). In this geometry, the damping-like SOT term $\sim \mathbf{m} \times (\mathbf{m} \times \boldsymbol{\sigma})$ is orthogonal to the damping term in the LLGS equation so it will have a negligible effect on the effective damping (SI Section 8). Instead, the effective DL-SOT field $\sim (\mathbf{m} \times \boldsymbol{\sigma})$ lies in the XZ plane causing a change in the equilibrium angle θ. Modulation of θ, in turn, leads to the modulation of the precessional frequency. This dependence is given by (SI Section 8):[45]

$$\frac{df}{dI_{dc}} = \frac{\mu_0\gamma}{4\pi}\left(\sqrt{\frac{H_2}{H_1}}\frac{\partial H_1}{\partial\theta} + \sqrt{\frac{H_1}{H_2}}\frac{\partial H_2}{\partial\theta}\right)\frac{\hbar\theta_{SH}}{2e\mu_0 M_s t_{FM} t_{HM} w H_2} \qquad (10)$$

Consequently, the efficiency of DL-SOT can be determined from the modulation of f by the electrical current.

Measuring the TR-MOKE signal in the presence of dc current, we observe a change in the frequency f due to the DL-SOT. Figure 3b shows a typical TR-MOKE time delay scan and its fitting by eq 2 for an external field of +400 mT applied at the angle of 15° ± 2° and zero dc current. The measured frequency of the TR-MOKE oscillations $f \sim 6.6$ GHz agrees with the frequency calculated from eq 5 using the experimental values of M_{eff}, H_{ex}, and θ_H. Figure 3c compares time delay scans for dc currents of +10 mA (red curve), 0 mA (black curve), and −10 mA (blue curve) and shows that the precession frequency increases for positive current and decreases for negative current. The detailed dependence of frequency on the dc current from −10 to +10 mA (Figure 3d) for $\mu_0 H_{ex} = +400$ mT confirms the frequency enhancement with current. To check that the linear modulation of the frequency is consistent with the DL-SOT, we reverse the external magnetic field to $\mu_0 H_{ex} = -400$ mT (Figure 2e) and observe that the reversal of the magnetic field does not change the sign of the linear slope $b = df/dI_{dc}$. This is understood because, under a field reversal, the precessional and DL-SOT terms transform with the same parity: $\mathbf{m} \times \mathbf{H}_{eff} \rightarrow +\mathbf{m} \times \mathbf{H}_{eff}$, $\mathbf{m} \times (\mathbf{m} \times \boldsymbol{\sigma}) \rightarrow +\mathbf{m} \times (\mathbf{m} \times \boldsymbol{\sigma})$. The frequency modulation data in Figure 3d,e are fitted using quadratic polynomials $aI_{dc}^2 + bI_{dc} + c$. The parabolic

term aI_{dc}^2 shows that Joule heating produces a frequency reduction, similar to W/CoFeB.[45] Using the obtained value of b, the effective spin Hall angle is calculated to be $\theta_{SH} = 0.066 \pm 0.014$ (SI Section 8). This agrees with the values measured by TR-MOKE damping modulation ($\theta_{SH} = 0.065 \pm 0.014$) and quasistatic MOKE ($\theta_{SH} = 0.059 \pm 0.010$). By obtaining consistent values from three independent measurements, we have systematically quantified the efficiency of DL-SOT.

Field-like SOT. Finally, we show that the field-like SOT is substantially weaker than the damping-like SOT in this study. We estimate the FL-SOT and in-plane Oersted field through two methods: (1) monitoring the in-plane hysteresis loop shift in the presence of an electrical current[48] and (2) frequency modulation of TR-MOKE in the standard geometry (discussed in SI Section 7). In the first method, we utilize longitudinal magnetic circular dichroism (MCD) with an oblique angle of incidence in a plane (XZ) perpendicular to the dc current (Y) (Figure 4a) (see SI Section 6 for experimental details). We chose longitudinal MCD over longitudinal MOKE because we found that it has a better signal-to-noise ratio in our experimental setup. As shown in Figure 4b, in the presence of a dc current, the Fe_3Sn_2 hysteresis loop is shifted due to the combination of the in-plane Oersted field and effective FL-SOT field (collinear with $\boldsymbol{\sigma}$). We estimate the FL-SOT contribution by calculating the in-plane Oersted field using Ampere's law $H_{IP}^{Oersted} = I_{dc}/2w$ and subtracting it from the measured shift ΔH_x. As shown in Figure 4c, the measured hysteresis loop shift can be almost fully accounted by the calculated in-plane Oersted field. The effective FL-SOT field normalized by current density is calculated to be $\mu_0 H_{FL}/j = -0.34 \pm 0.25$ mT per 10^{12} A/m^2, which is ~20 times smaller than the value measured for the DL-SOT. This is consistent with previous studies on the conventional FM/HM bilayer that found the FL-SOT to be small for films with the thickness of a magnetic layer larger than ~1−2 nm.[36,48−51] This also agrees with the value of $\mu_0 H_{FL}/j = -0.4 \pm 0.7$ mT per 10^{12} A/m^2 obtained using TR-MOKE (SI Section 7).

CONCLUSION

In summary, we observed spin−orbit torque in epitaxial bilayers of the kagome ferromagnet Fe_3Sn_2 and Pt. Using quasistatic polar MOKE, we determined the efficiency of DL-SOT by spatially mapping the induced changes in the out-of-plane magnetization while applying an electric current. In the TR-MOKE study, we measured the efficiency of DL-SOT in two different geometries where the SOT produces changes in either the damping or the precessional frequency. Analysis of these independent measurements generates consistent results for the effective spin Hall angle θ_{SH} (~6%). In addition, we showed that the FL-SOT is much smaller than the DL-SOT in our study. These results establish spin−orbit torque in epitaxial kagome ferromagnet Fe_3Sn_2/Pt bilayers and facilitate the development of spintronics based on topological kagome magnets.

ASSOCIATED CONTENT

ⓢ Supporting Information

The Supporting Information is available free of charge at https://pubs.acs.org/doi/10.1021/acs.nanolett.1c02270.

> Experimental methods (MBE growth, device fabrication and transport characterization, magneto-optical measurements), determination of FL-SOT by TR-MOKE,

and derivation of the SOT-induced damping and frequency modulation equations from the LLGS equation (PDF)

AUTHOR INFORMATION

Corresponding Author
Roland K. Kawakami − *Department of Physics, The Ohio State University, Columbus, Ohio 43210, United States;* ⓘ orcid.org/0000-0003-0245-9192; Email: kawakami.15@osu.edu

Authors
Igor Lyalin − *Department of Physics, The Ohio State University, Columbus, Ohio 43210, United States*
Shuyu Cheng − *Department of Physics, The Ohio State University, Columbus, Ohio 43210, United States*

Complete contact information is available at:
https://pubs.acs.org/10.1021/acs.nanolett.1c02270

Author Contributions
‡(I.L. and S.C.) These authors contributed equally.

Author Contributions
I.L., S.C., and R.K.K. conceived the experiments. I.L. performed the device fabrication and magneto-optical measurements. S.C. performed MBE growth of the samples. All authors participated in data analysis and preparation of the manuscript.

Notes
The authors declare no competing financial interest.

REFERENCES

(1) Taguchi, Y.; Oohara, Y.; Yoshizawa, H.; Nagaosa, N.; Tokura, Y. Spin Chirality, Berry Phase, and Anomalous Hall Effect in a Frustrated Ferromagnet. *Science* **2001**, *291*, 2573−2576.
(2) Fenner, L. A.; Dee, A. A.; Wills, A. S. Non-collinearity and spin frustration in the itinerant kagome ferromagnet Fe_3Sn_2. *J. Phys.: Condens. Matter* **2009**, *21*, 452202.
(3) Nakatsuji, S.; Kiyohara, N.; Higo, T. Large anomalous Hall effect in a non-collinear antiferromagnet at room temperature. *Nature* **2015**, *527*, 212−215.
(4) Jeong, M.; Bert, F.; Mendels, P.; Duc, F.; Trombe, J. C.; de Vries, M. A.; Harrison, A. Field-Induced Freezing of a Quantum Spin Liquid on the Kagome Lattice. *Phys. Rev. Lett.* **2011**, *107*, 237201.
(5) Han, T.-H.; Helton, J. S.; Chu, S.; Nocera, D. G.; Rodriguez-Rivera, J. A.; Broholm, C.; Lee, Y. S. Fractionalized excitations in the spin-liquid state of a kagome-lattice antiferromagnet. *Nature* **2012**, *492*, 406−410.
(6) Pereiro, M.; Yudin, D.; Chico, J.; Etz, C.; Eriksson, O.; Bergman, A. Topological excitations in a kagome magnet. *Nat. Commun.* **2014**, *5*, 4815.
(7) Hou, Z.; Ren, W.; Ding, B.; Xu, G.; Wang, Y.; Yang, B.; Zhang, Q.; Zhang, Y.; Liu, E.; Xu, F.; Wang, W.; Wu, G.; Zhang, X.; Shen, B.; Zhang, Z. Observation of Various and Spontaneous Magnetic Skyrmionic Bubbles at Room Temperature in a Frustrated Kagome Magnet with Uniaxial Magnetic Anisotropy. *Adv. Mater.* **2017**, *29*, 1701144.
(8) Hou, Z.; Zhang, Q.; Xu, G.; Zhang, S.; Gong, C.; Ding, B.; Li, H.; Xu, F.; Yao, Y.; Liu, E.; Wu, G.; Zhang, X.-x.; Wang, W.

Manipulating the Topology of Nanoscale Skyrmion Bubbles by Spatially Geometric Confinement. *ACS Nano* **2019**, *13*, 922−929.

(9) Hirschberger, M.; et al. Skyrmion phase and competing magnetic orders on a breathing kagomé lattice. *Nat. Commun.* **2019**, *10*, 5831.

(10) Tang, J.; Kong, L.; Wu, Y.; Wang, W.; Chen, Y.; Wang, Y.; Li, J.; Soh, Y.; Xiong, Y.; Tian, M.; Du, H. Target Bubbles in Fe₃Sn₂ Nanodisks at Zero Magnetic Field. *ACS Nano* **2020**, *14*, 10986−10992.

(11) Kuroda, K.; et al. Evidence for magnetic Weyl fermions in a correlated metal. *Nat. Mater.* **2017**, *16*, 1090−1095.

(12) Ye, L.; Kang, M.; Liu, J.; von Cube, F.; Wicker, C. R.; Suzuki, T.; Jozwiak, C.; Bostwick, A.; Rotenberg, E.; Bell, D. C.; Fu, L.; Comin, R.; Checkelsky, J. G. Massive Dirac fermions in a ferromagnetic kagome metal. *Nature* **2018**, *555*, 638−642.

(13) Yin, J.-X.; et al. Giant and anisotropic many-body spin−orbit tunability in a strongly correlated kagome magnet. *Nature* **2018**, *562*, 91−95.

(14) Kang, M.; et al. Dirac fermions and flat bands in the ideal kagome metal FeSn. *Nat. Mater.* **2020**, *19*, 163−169.

(15) Kida, T.; Fenner, L. A.; Dee, A. A.; Terasaki, I.; Hagiwara, M.; Wills, A. S. The giant anomalous Hall effect in the ferromagnet Fe₃Sn₂—a frustrated kagome metal. *J. Phys.: Condens. Matter* **2011**, *23*, 112205.

(16) Nayak, A. K.; Fischer, J. E.; Sun, Y.; Yan, B.; Karel, J.; Komarek, A. C.; Shekhar, C.; Kumar, N.; Schnelle, W.; Kübler, J.; Felser, C.; Parkin, S. S. P. Large anomalous Hall effect driven by a nonvanishing Berry curvature in the noncolinear antiferromagnet Mn₃Ge. *Science Advances* **2016**, *2*, No. e1501870.

(17) Liu, E.; et al. Giant anomalous Hall effect in a ferromagnetic kagome-lattice semimetal. *Nat. Phys.* **2018**, *14*, 1125−1131.

(18) Ikhlas, M.; Tomita, T.; Koretsune, T.; Suzuki, M.-T.; Nishio-Hamane, D.; Arita, R.; Otani, Y.; Nakatsuji, S. Large anomalous Nernst effect at room temperature in a chiral antiferromagnet. *Nat. Phys.* **2017**, *13*, 1085−1090.

(19) Guin, S. N.; Vir, P.; Zhang, Y.; Kumar, N.; Watzman, S. J.; Fu, C.; Liu, E.; Manna, K.; Schnelle, W.; Gooth, J.; Shekhar, C.; Sun, Y.; Felser, C. Zero-Field Nernst Effect in a Ferromagnetic Kagome-Lattice Weyl-Semimetal Co₃Sn₂S₂. *Adv. Mater.* **2019**, *31*, 1806622.

(20) Khadka, D.; Thapaliya, T. R.; Hurtado Parra, S.; Wen, J.; Need, R.; Kikkawa, J. M.; Huang, S. X. Anomalous Hall and Nernst effects in epitaxial films of topological kagome magnet Fe₃Sn₂. *Phys. Rev. Materials* **2020**, *4*, 084203.

(21) Chen, T.; Tomita, T.; Minami, S.; Fu, M.; Koretsune, T.; Kitatani, M.; Muhammad, I.; Nishio-Hamane, D.; Ishii, R.; Ishii, F.; Arita, R.; Nakatsuji, S. Anomalous transport due to Weyl fermions in the chiral antiferromagnets Mn₃X, X = Sn, Ge. *Nat. Commun.* **2021**, *12*, 572.

(22) Yao, M.; Lee, H.; Xu, N.; Wang, Y.; Ma, J.; Yazyev, O. V.; Xiong, Y.; Shi, M.; Aeppli, G.; Soh, Y. Switchable Weyl nodes in topological Kagome ferromagnet Fe₃Sn₂. *arXiv [cond-mat.str-el]*, 2018, 1810.01514. http://arxiv.org/abs/1810.01514 (accessed May 7, 2021).

(23) Šmejkal, L.; Mokrousov, Y.; Yan, B.; MacDonald, A. H. Topological antiferromagnetic spintronics. *Nat. Phys.* **2018**, *14*, 242−251.

(24) Manchon, A.; Železný, J.; Miron, I.; Jungwirth, T.; Sinova, J.; Thiaville, A.; Garello, K.; Gambardella, P. Current-induced spin-orbit torques in ferromagnetic and antiferromagnetic systems. *Rev. Mod. Phys.* **2019**, *91*, 035004.

(25) Demidov, V. E.; Urazhdin, S.; Ulrichs, H.; Tiberkevich, V.; Slavin, A.; Baither, D.; Schmitz, G.; Demokritov, S. O. Magnetic nano-oscillator driven by pure spin current. *Nat. Mater.* **2012**, *11*, 1028−1031.

(26) Emori, S.; Bauer, U.; Ahn, S.-M.; Martinez, E.; Beach, G. S. D. Current-driven dynamics of chiral ferromagnetic domain walls. *Nat. Mater.* **2013**, *12*, 611−616.

(27) Jiang, W.; Upadhyaya, P.; Zhang, W.; Yu, G.; Jungfleisch, M. B.; Fradin, F. Y.; Pearson, J. E.; Tserkovnyak, Y.; Wang, K. L.; Heinonen, O.; te Velthuis, S. G. E.; Hoffmann, A. Blowing magnetic skyrmion bubbles. *Science* **2015**, *349*, 283−286.

(28) Miron, I. M.; Garello, K.; Gaudin, G.; Zermatten, P.-J.; Costache, M. V.; Auffret, S.; Bandiera, S.; Rodmacq, B.; Schuhl, A.; Gambardella, P. Perpendicular switching of a single ferromagnetic layer induced by in-plane current injection. *Nature* **2011**, *476*, 189−193.

(29) Liu, L.; Pai, C.-F.; Li, Y.; Tseng, H. W.; Ralph, D. C.; Buhrman, R. A. Spin-Torque Switching with the Giant Spin Hall Effect of Tantalum. *Science* **2012**, *336*, 555−558.

(30) Fukami, S.; Anekawa, T.; Zhang, C.; Ohno, H. A spin−orbit torque switching scheme with collinear magnetic easy axis and current configuration. *Nat. Nanotechnol.* **2016**, *11*, 621−625.

(31) Soumyanarayanan, A.; Reyren, N.; Fert, A.; Panagopoulos, C. Emergent phenomena induced by spin−orbit coupling at surfaces and interfaces. *Nature* **2016**, *539*, 509−517.

(32) Fert, A.; Reyren, N.; Cros, V. Magnetic skyrmions: advances in physics and potential applications. *Nature Reviews Materials* **2017**, *2*, 17031.

(33) Tsai, H.; Higo, T.; Kondou, K.; Nomoto, T.; Sakai, A.; Kobayashi, A.; Nakano, T.; Yakushiji, K.; Arita, R.; Miwa, S.; Otani, Y.; Nakatsuji, S. Electrical manipulation of a topological antiferro-magnetic state. *Nature* **2020**, *580*, 608−613.

(34) Takeuchi, Y.; Yamane, Y.; Yoon, J.-Y.; Itoh, R.; Jinnai, B.; Kanai, S.; Ieda, J.; Fukami, S.; Ohno, H. Chiral-spin rotation of non-collinear antiferromagnet by spin−orbit torque. *Nat. Mater.* **2021**, DOI: 10.1038/s41563-021-01005-3.

(35) Cheng, S.; Lyalin, I.; Bishop, A. J.; Kawakami, R. K. Epitaxial Growth and Domain Structure Imaging of Kagome Magnet Fe₃Sn₂. *arXiv [cond-mat.mtrl-sci]*, 2021, 2105.12203. http://arxiv.org/abs/2105.12203 (accessed June 8, 2021).

(36) Fan, X.; Celik, H.; Wu, J.; Ni, C.; Lee, K.-J.; Lorenz, V. O.; Xiao, J. Q. Quantifying interface and bulk contributions to spin−orbit torque in magnetic bilayers. *Nat. Commun.* **2014**, *5*, 3042.

(37) Fan, X.; Mellnik, A. R.; Wang, W.; Reynolds, N.; Wang, T.; Celik, H.; Lorenz, V. O.; Ralph, D. C.; Xiao, J. Q. All-optical vector measurement of spin-orbit-induced torques using both polar and quadratic magneto-optic Kerr effects. *Appl. Phys. Lett.* **2016**, *109*, 122406.

(38) Ando, K.; Takahashi, S.; Harii, K.; Sasage, K.; Ieda, J.; Maekawa, S.; Saitoh, E. Electric Manipulation of Spin Relaxation Using the Spin Hall Effect. *Phys. Rev. Lett.* **2008**, *101*, 036601.

(39) Liu, L.; Moriyama, T.; Ralph, D. C.; Buhrman, R. A. Spin-Torque Ferromagnetic Resonance Induced by the Spin Hall Effect. *Phys. Rev. Lett.* **2011**, *106*, 036601.

(40) Beaurepaire, E.; Merle, J.-C.; Daunois, A.; Bigot, J.-Y. Ultrafast Spin Dynamics in Ferromagnetic Nickel. *Phys. Rev. Lett.* **1996**, *76*, 4250−4253.

(41) van Kampen, M.; Jozsa, C.; Kohlhepp, J. T.; LeClair, P.; Lagae, L.; de Jonge, W. J. M.; Koopmans, B. All-Optical Probe of Coherent Spin Waves. *Phys. Rev. Lett.* **2002**, *88*, 227201.

(42) Mizukami, S.; Wu, F.; Sakuma, A.; Walowski, J.; Watanabe, D.; Kubota, T.; Zhang, X.; Naganuma, H.; Oogane, M.; Ando, Y.; Miyazaki, T. Long-Lived Ultrafast Spin Precession in Manganese Alloys Films with a Large Perpendicular Magnetic Anisotropy. *Phys. Rev. Lett.* **2011**, *106*, 117201.

(43) Ganguly, A.; Rowan-Robinson, R. M.; Haldar, A.; Jaiswal, S.; Sinha, J.; Hindmarch, A. T.; Atkinson, D. A.; Barman, A. Time-domain detection of current controlled magnetization damping in Pt/Ni₈₁Fe₁₉ bilayer and determination of Pt spin Hall angle. *Appl. Phys. Lett.* **2014**, *105*, 112409.

(44) Mondal, S.; Choudhury, S.; Jha, N.; Ganguly, A.; Sinha, J.; Barman, A. All-optical detection of the spin Hall angle in W/CoFeB/SiO₂ heterostructures with varying thickness of the tungsten layer. *Phys. Rev. B: Condens. Matter Mater. Phys.* **2017**, *96*, 054414.

(45) Ishibashi, K.; Iihama, S.; Takeuchi, Y.; Furuya, K.; Kanai, S.; Fukami, S.; Mizukami, S. All-optical probe of magnetization precession modulated by spin−orbit torque. *Appl. Phys. Lett.* **2020**, *117*, 122403.

(46) Heinrich, B. In *Ultrathin Magnetic Structures III: Fundamentals of Nanomagnetism*; Bland, J. A. C., Heinrich, B., Eds.; Springer: Berlin, Heidelberg, 2005; pp 143−210.

(47) Frait, Z.; Fraitova, D. *Low Energy Spin-Wave Excitation in Highly Conductive Thin Films and Surfaces. Frontiers in Magnetism of Reduced Dimension Systems*; Springer: Dordrecht, 1998; pp 121−151.

(48) Fan, X.; Wu, J.; Chen, Y.; Jerry, M. J.; Zhang, H.; Xiao, J. Q. Observation of the nonlocal spin-orbital effective field. *Nat. Commun.* **2013**, *4*, 1799.

(49) Kim, J.; Sinha, J.; Hayashi, M.; Yamanouchi, M.; Fukami, S.; Suzuki, T.; Mitani, S.; Ohno, H. Layer thickness dependence of the current-induced effective field vector in Ta/CoFeB/MgO. *Nat. Mater.* **2013**, *12*, 240−245.

(50) Skinner, T. D.; Wang, M.; Hindmarch, A. T.; Rushforth, A. W.; Irvine, A. C.; Heiss, D.; Kurebayashi, H.; Ferguson, A. J. Spin-orbit torque opposing the Oersted torque in ultrathin Co/Pt bilayers. *Appl. Phys. Lett.* **2014**, *104*, 062401.

(51) Avci, C. O.; Garello, K.; Gabureac, M.; Ghosh, A.; Fuhrer, A.; Alvarado, S. F.; Gambardella, P. Interplay of spin-orbit torque and thermoelectric effects in ferromagnet/normal-metal bilayers. *Phys. Rev. B: Condens. Matter Mater. Phys.* **2014**, *90*, 224427.